Hindawi
Shock and Vibration
Volume 2022, Article ID 4308193, 10 pages
https://doi.org/10.1155/2022/4308193

Research Article

PPV Criterion of a Defect Rock Slope under Blasting SV-Waves

Shiwei Lu,[1,2] **Yingkang Yao**,[1,3] **Yongsheng Jia**,[1,3] **Jinshan Sun**,[1,3] **and Zhen Zhang**[1,3]

[1]*State Key Laboratory of Precision Blasting, Jianghan University, Wuhan 430056, China*
[2]*School of Urban Construction, Yangtze University, Jingzhou 434023, Hubei, China*
[3]*Hubei Key Laboratory of Blasting Engineering, Jianghan University, Wuhan 430056, China*

Correspondence should be addressed to Yingkang Yao; shanxiyao@jhun.edu.cn

Received 13 May 2022; Revised 20 July 2022; Accepted 6 October 2022; Published 28 October 2022

Academic Editor: Chang-Ping Yi

Copyright © 2022 Shiwei Lu et al. This is an open access article distributed under the Creative Commons Attribution License, which permits unrestricted use, distribution, and reproduction in any medium, provided the original work is properly cited.

In order to estimate the stability of slopes with geological defects during blasting excavations, the dynamic responses of a rock slope with a fault subjected to blasting seismic waves are studied. The SV-component of blasting seismic waves is considered and the fault is simplified as a semi-infinite crack in an unbounded space. In the background of an iron mine in central China, the relation between the stress field and the PPV of the incident wave is analyzed and the function of PPV threshold is deduced using both deterministic and probabilistic methods to evaluate the slope stability. Results show that the PPV threshold increases monotonically with the increasing frequency and reaches the lowest point at around $\gamma_1 = 14^\circ$, which should be proposed as the PPV threshold. The PPV threshold is with an about 50% failure probability when the mean values of mechanical parameters are taken. On the safe side, a more rigorous PPV threshold with only 5% failure probability is determined as 2.25 cm/s for $f \leq 10$ Hz, as 2.25 cm/s-5.02 cm/s for 10 Hz $< f \leq 50$ Hz, and as 5.02 cm/s-10.05 cm/s for $f > 50$ Hz. A through structural surface is likely to occur inside the northern slope once the PPV exceeds the proposed threshold.

1. Introduction

With the increasing demand for mineral resources and the depletion of near-surface ones, underground mining is the only viable option. Consequently, more and more slopes with defects, such as faults and discontinuities, will possess a declining stability due to the disturbance of underground mining operations. On the other hand, the drilling-blasting method is still one of the most effective means for mining. During the mining process, the stability of slopes inevitably disturbed by blasting waves will reduce further, which may lead to catastrophic hazards. Therefore, studies on the dynamic responses of slopes and the dynamic stability evaluation have drawn considerable attention and become increasingly significant in geotechnical engineering.

For decades, a massive number of studies on the dynamic stability of slopes have been conducted. Feng et al. discussed the dynamic responses of an antidip rock slope containing two groups of rock joints and estimated its stability by shaking table test [1]. Huang et al. analyzed the impact of oblique incident earthquake excitations using the equivalent nodal force method [2]. Compared with the physical model test and theoretical analysis, the numerical method has been widely used to study the slope stability for its economy and applicability to complex problems. Perth et al. revealed the stability of rock slopes subjected to underground blasting by the finite difference method [3]. Fan et al. proposed a new seismic input method in numerical simulations and investigated the dynamic response of rock slopes subjected to oblique incident SV-waves [4]. Ganjeh et al. compared the effects of earthquake and blasting on the stability of the NW slope of the Chadormalu mine [5]. Zhang et al. established a numerical model to estimate the effects of tension failure on seismic slope stability [6]. Liu et al. adopted the dynamic limit equilibrium solution to analyze the stability of a potential sliding block based on the finite element method [7]. Deb et al. studied the dynamic stability of the rock slope in the Pasir mine based on the numerical simulations and in situ vibration tests and suggested possible causes of slope failures [8]. However, most of these studies were without considering the geological defects which actually exist and play an even critical role. It is very necessary

to investigate the dynamic response of these defected slopes and to evaluate the stability. In blasting engineering, the peak particle velocity (PPV) is conventionally selected as a measure of vibration intensity to estimate the influence of blasting activities [9–12]. Lu et al. proposed the PPV threshold of a rock slope imbedded with a fault under blasting P-waves in theory [13].

Since the fault tip is always deeply buried, we have reason to believe the dynamic response induced by body waves (including P- and S-waves) is more serious than surface waves. Besides, the blasting seismic wave can be approximately considered as a plane wave and then the proposed PPV is basically immune to the distance after a certain standoff distance [14]. In this paper, the fault is simplified as a semi-infinite crack in an infinite space, and the SV-component of blasting seismic waves is extracted as a plane wave to study the dynamic responses of a jointed rock slope based on the dynamic fracture mechanics. Moreover, the relation between the stress field and the PPV of the incident wave is analyzed and the function of PPV threshold is deduced to evaluate the slope stability. The PPV thresholds using deterministic and probabilistic methods are compared in the background of an iron reserve in central China. Finally, the proposed PPV threshold for different frequency intervals is recommended in accordance with the safety regulations for blasting in China.

2. Interaction of SV-Wave and Fault

2.1. Simplified Model. A right-handed Cartesian coordinate system Oxy is established as shown in Figure 1. Assume a semi-infinite crack lies in the negative x-axis extending from $-\infty$ to 0 and the crack tip is at the original point. The crack is impinged by a time harmonic plane incident SV-wave at the angle γ_1. Meanwhile, a polar coordinate system (r, θ) is also set up to analyze the stress field near the crack tip. The potential function of the incident time-harmonic plane SV-wave can be expressed as follows:

$$\psi^{(i)}(x, y, t) = \psi_0 \exp\left[-i\alpha_1\left(x\cos\gamma_1 + y\sin\gamma_1\right) - i\omega t\right], \quad (1)$$

where ψ_0 is the amplitude of the incident SV-wave, α_1 is the wave number of SV-wave and equal to the ratio of ω (circular frequency of incident wave) to c_1 (wave speed of SV-wave and $c_1 = \sqrt{E(\xi)/2\rho[1+\upsilon(\xi)]}$), E is Young's modulus, υ is Poisson's ratio, ρ is the density of rock mass, i is the unit of complex, and E and υ are considered as random functions of a random variable ξ.

In general, two types of diffracted waves will be generated when the plane SV-wave arrives at the crack. They are the diffracted P-wave ($\varphi^{(d)}$) and the diffracted SV-wave ($\psi^{(d)}$). Let φ denote the potential of the diffracted P-wave and ψ the sum of potentials of the incident and the diffracted SV-waves, that is,

$$\begin{cases} \psi(x, y, t) = \psi^{(i)}(x, y, t) + \psi^{(d)}(x, y, t), \\ \phi(x, y, t) = \phi^{(d)}(x, y, t), \end{cases} \quad (2)$$

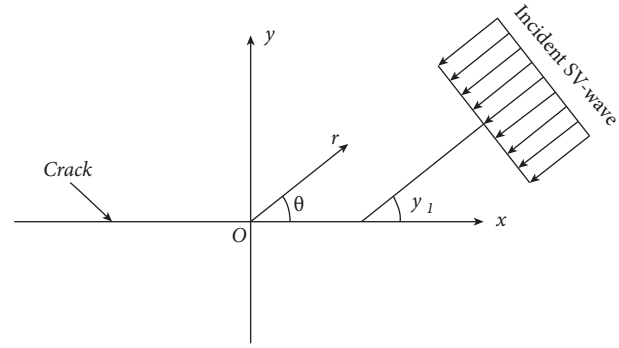

Figure 1: Interaction between SV-wave and fault.

where the diffracted field must satisfy the radiation conditions: $\varphi^{(d)}, \psi^{(d)} \longrightarrow 0$ as $(x^2+y^2)^{1/2} \longrightarrow \infty$.

The total field must obey the following governing equations:

$$\begin{cases} \nabla^2\psi = \dfrac{1}{c_1^2}\dfrac{\partial^2\psi}{\partial t^2}, \\ \nabla^2\varphi = \dfrac{1}{c_2^2}\dfrac{\partial^2\varphi}{\partial t^2}, \end{cases} \quad (3)$$

where c_2 is the wave speed of P-wave and $c_2 = \sqrt{E[1-\upsilon(\xi)]/\rho[1+\upsilon(\xi)][1-2\upsilon(\xi)]}$.

The displacement and stress components can be expressed by potential functions as follows:

$$\begin{cases} u_x = \dfrac{\partial\varphi}{\partial x} + \dfrac{\partial\psi}{\partial y}, \\ u_y = \dfrac{\partial\varphi}{\partial y} - \dfrac{\partial\psi}{\partial x}, \\ \sigma_{xx} = \lambda\nabla^2\varphi + 2\mu\left(\dfrac{\partial^2\varphi}{\partial x^2} + \dfrac{\partial^2\psi}{\partial x\partial y}\right), \\ \sigma_{yy} = \lambda\nabla^2\varphi + 2\mu\left(\dfrac{\partial^2\varphi}{\partial y^2} - \dfrac{\partial^2\psi}{\partial x\partial y}\right), \\ \sigma_{xy} = \mu\left(2\dfrac{\partial^2\varphi}{\partial x\partial y} - \dfrac{\partial^2\psi}{\partial x^2} + \dfrac{\partial^2\psi}{\partial y^2}\right). \end{cases} \quad (4)$$

The diffracted waves should be time harmonic since the incident SV-wave is time harmonic. As a result, the potentials can be expressed as follows:

$$\begin{cases} \psi^{(d)}(x, y, t) = \widehat{\psi}^{(d)}(x, y)\exp(-i\omega t), \\ \varphi^{(d)}(x, y, t) = \widehat{\varphi}^{(d)}(x, y)\exp(-i\omega t), \end{cases} \quad (5)$$

where $\widehat{\psi}^{(d)}(x, y)$ and $\widehat{\varphi}^{(d)}(x, y)$ are governed by the following Helmholtz equations:

$$\begin{cases} \left(\nabla^2 + \alpha_1^2\right)\widehat{\psi}^d(x,y) = 0, \\ \left(\nabla^2 + \alpha_2^2\right)\widehat{\varphi}^d(x,y) = 0. \end{cases} \tag{6}$$

The boundary conditions are given by:

$$\begin{cases} \sigma_{yy}^{(i)}(x,0,t) + \sigma_{yy}^{(d)}(x,0,t) = 0, \\ \sigma_{xy}^{(i)}(x,0,t) + \sigma_{yy}^{(d)}(x,0,t) = 0, \end{cases} \quad x < 0. \tag{7}$$

For convenience, the abovementioned problem can be divided into a symmetric part with respect to the x-axis and an antisymmetric part. Consequently, the division also holds for diffracted fields: $\psi^{(s)}, \varphi^{(s)}$ are symmetric and $\psi^{(a)}, \varphi^{(a)}$ are antisymmetric. The free surfaces inside the crack and the intact part outside the crack are subjected to the following boundary conditions:

$$\begin{cases} \sigma_{xy}^{(s)}(x,0,t) = 0, u_y^{(s)}(x,0,t) = 0, & x > 0, \\ \sigma_{yy}^{(i)}(x,0,t) + \sigma_{yy}^{(s)}(x,0,t) = 0, \sigma_{xy}^{(s)}(x,0,t) = 0, & x < 0, \end{cases} \tag{8}$$

for the symmetric part and

$$\begin{cases} \sigma_{yy}^{(a)}(x,0,t) = 0, u_x^{(a)}(x,0,t) = 0, & x > 0, \\ \sigma_{xy}^{(i)}(x,0,t) + \sigma_{xy}^{(a)}(x,0,t) = 0, \sigma_{yy}^{(a)}(x,0,t) = 0 & x < 0, \end{cases} \tag{9}$$

for the antisymmetric part. Applying Fourier transforms to the space variable x, the solutions can be obtained in terms of the transformed variable s.

$$\begin{cases} \psi^{(s)}(x,y,t) = \dfrac{1}{2\pi}\displaystyle\int_{-\infty}^{+\infty} A_{11}(s) e^{-\beta_1|y| - isx - i\omega t} ds, \\ \phi^{(s)}(x,y,t) = \dfrac{1}{2\pi}\displaystyle\int_{-\infty}^{+\infty} A_{12}(s) e^{-\beta_2|y| - isx - i\omega t} ds, \\ \psi^{(a)}(x,y,t) = \dfrac{1}{2\pi}\displaystyle\int_{-\infty}^{+\infty} A_{21}(s) e^{-\beta_1|y| - isx - i\omega t} ds, \\ \phi^{(a)}(x,y,t) = \dfrac{1}{2\pi}\displaystyle\int_{-\infty}^{+\infty} A_{22}(s) e^{-\beta_2|y| - isx - i\omega t} ds, \end{cases} \tag{10}$$

where $\beta_j = \begin{cases} \sqrt{s^2 - \alpha_j^2} & |s| \geq \alpha_j \\ -i\sqrt{\alpha_j^2 - s^2} & |s| < \alpha_j \end{cases}$, $j = 1, 2$ in order to determine the outgoing waves and obtain the unique solution, and $A_{j1}(s)$ and $A_{j2}(s)$are determined from boundary conditions. The integral path is shown in Figure 2.

Let $\begin{pmatrix} A_{11}(s) \\ A_{12}(s) \end{pmatrix} = 2/\alpha_1^2 A_1(s) \begin{pmatrix} s^2 - 1/2\alpha_1^2 \\ -is\beta_2 \end{pmatrix}$ and $\begin{pmatrix} A_{21}(s) \\ A_{22}(s) \end{pmatrix} = 2/\alpha_1^2 A_2(s) \begin{pmatrix} is\beta_1 \\ s^2 - 1/2\alpha_1^2 \end{pmatrix}$, the boundary conditions can be derived as the following dual integral equations:

$$\begin{cases} \dfrac{1}{2\pi}\displaystyle\int_{-\infty}^{+\infty} \beta_1 A_1(s) \exp(-isx) ds = 0, & x > 0, \\ \dfrac{1}{2\pi}\displaystyle\int_{-\infty}^{+\infty} f(s) A_1(s) \exp(-isx) ds = P_1 \exp\left(-i\alpha_1 x \cos\gamma_1\right), & x < 0, \end{cases} \tag{11}$$

$$\begin{cases} \dfrac{1}{2\pi}\displaystyle\int_{-\infty}^{+\infty} \beta_2 A_2(s) \exp(-isx) ds = 0, & x > 0, \\ \dfrac{1}{2\pi}\displaystyle\int_{-\infty}^{+\infty} f(s) A_2(s) \exp(-isx) ds = Q_1 \exp\left(-i\alpha_1 x \cos\gamma_1\right), & x < 0, \end{cases} \tag{12}$$

where $P_1 = -\alpha_1^4 \psi_0 \sin 2\gamma_1$, $Q_1 = -\alpha_1^4 \psi_0 \cos 2\gamma_1$, and $f(s) = (2s^2 - \alpha_1^2)^2 - 4s^2\beta_1\beta_2$.

Equations (11) and (12) can be solved by the Wiener–Hopf technique [15, 16], and the results can be expressed as follows:

$$\begin{cases} A_1(s) = -\dfrac{P_1}{2i} \cdot \dfrac{\sqrt{\alpha_1 + \alpha_1\cos\gamma_1}}{\left(\alpha_1^2 - \alpha_2^2\right)(\alpha_R + \alpha_1\cos\gamma_1) F_+(\alpha_1\cos\gamma_1)} \cdot \dfrac{1}{(s - \alpha_R)(s - \alpha_1\cos\gamma_1)\sqrt{s + \alpha_2}\, F_-(s)}, \\ A_2(s) = -\dfrac{Q_1}{2i} \cdot \dfrac{\sqrt{\alpha_1 + \alpha_1\cos\gamma_1}}{\left(\alpha_1^2 - \alpha_2^2\right)(\alpha_R + \alpha_1\cos\gamma_1) F_+(\alpha_1\cos\gamma_1)} \cdot \dfrac{1}{(s - \alpha_R)(s - \alpha_1\cos\gamma_1)\sqrt{s + \alpha_1}\, F_-(s)}, \end{cases} \tag{13}$$

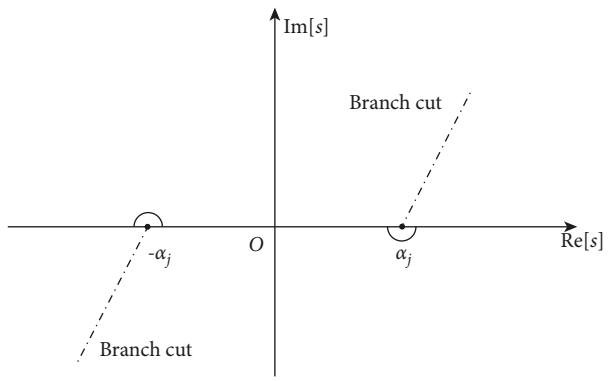

Figure 2: Integral path in s-plane.

where $F_{\pm}(s) = \exp\left\{1\pi \int_{\alpha_1}^{\alpha_2} \arctan\left(4z^2\sqrt{(z^2-\alpha_1^2)(\alpha_2^2-z^2)}\,/\,(2z^2-\alpha_1^2)^2\right)(dz/z+s)\right\}$ and α_R is the wave number of Rayleigh wave and given by the minimum positive real root of the equation $(2-\alpha_1^2/\alpha_R^2)^2 - 4\sqrt{(1-\alpha_1^2/\alpha_R^2)(1-\alpha_2^2/\alpha_R^2)} = 0$.

Because the incident wave will not cause the stress singularity in the vicinity of crack tip, the near-field stress components are only determined by the diffracted waves. Then the mode I stress intensity factor (SIF) is expressed as follows:

$$K_I = \lim_{x \longrightarrow 0} \sqrt{2\pi x}\sigma_{yy}(x,0,t) = \tau\sqrt{\pi\lambda_1}\left|K_I^{(1)}\right| \exp\left[-i\left(\omega t + \frac{3\pi}{4}\right)\right], \tag{14}$$

and the mode II SIF is expressed as follows:

$$K_{II} = \lim_{x \longrightarrow 0} \sqrt{2\pi x}\sigma_{xy}(x,0,t) = \tau\sqrt{\pi\lambda_1}\left|K_{II}^{(1)}\right| \exp\left[-i\left(\omega t + \frac{3\pi}{4}\right)\right], \tag{15}$$

where $\tau = \mu\alpha_1^2\psi_0$ and $K_I^{(1)} = \sin 2\gamma_1\sqrt{\kappa+\cos\gamma_1}/\pi(\alpha_R/\alpha_1 + \cos\gamma_1)F_+(\alpha_1\cos\gamma_1)$,

$$K_{II}^{(1)} = \frac{\cos 2\gamma_1\sqrt{1+\cos\gamma_1}}{\pi(\alpha_R/\alpha_1+\cos\gamma_1)F_+(\alpha_1\cos\gamma_1).} \tag{16}$$

The PPV parallel to the wavefront of the incident wave can be expressed as follows:

$$v_{\mathrm{SV}} = \omega\alpha_1\psi_0. \tag{17}$$

Substituting equation (17) into equations (14) and (15), we can obtain the SIFs in terms of v_{SV} as follows:

$$\begin{aligned} K_I &= \frac{\mu v_{SV}\alpha_1}{\omega}\sqrt{\pi\lambda_1}\left|K_I^{(1)}\right| \exp\left[-i\left(\omega t + \frac{3\pi}{4}\right)\right], \\ K_{II} &= \frac{\mu v_{SV}\alpha_1}{\omega}\sqrt{\pi\lambda_1}\left|K_{II}^{(1)}\right| \exp\left[-i\left(\omega t + \frac{3\pi}{4}\right)\right]. \end{aligned} \tag{18}$$

2.2. Safety Criterion Model. When a plane SV-wave arrives at the crack tip, the stress field in the vicinity of crack tip can be expressed as follows [11]:

$$\begin{cases} \sigma_{rr} = \dfrac{1}{2\sqrt{2\pi r}}\left[K_I(3-\cos\theta)\cos\dfrac{\theta}{2} + K_{II}(3\cos\theta-1)\sin\dfrac{\theta}{2}\right], \\ \sigma_{\theta\theta} = \dfrac{1}{2\sqrt{2\pi r}}\cos\dfrac{\theta}{2}\left[K_I(1+\cos\theta) - 3K_{II}\sin\theta\right], \\ \sigma_{r\theta} = \dfrac{1}{2\sqrt{2\pi r}}\cos\dfrac{\theta}{2}\left[K_I\sin\theta + K_{II}(3\cos\theta-1)\right], \\ \sigma_{zz} = \upsilon(\sigma_{rr}+\sigma_{\theta\theta}), \\ \sigma_{rz} = \sigma_{\theta z} = 0, \end{cases} \tag{19}$$

where υ is Poisson's ratio.

The maximum circumferential tensile stress criterion is always adopted to analyze fracture cracking. As a consequence, the PPV threshold can be expressed as follows:

$$v_{\mathrm{SV}} = 2\omega K_{IC}(\xi)\mu\alpha_1\sqrt{\pi\lambda_1} \cos\frac{\theta_0}{2}\left[\left|K_I^{(1)}\right|(1+\cos\theta_0) - 3\sin\theta_0\left|K_{II}^{(1)}\right|\right], \tag{20}$$

where θ_0 is the initiation angle and $\theta_0 = 2\arctan 1 - \sqrt{1+8(|K_{II}^{(1)}|/|K_I^{(1)}|)^2}/4|K_{II}^{(1)}|/|K_I^{(1)}|$ and K_{IC} is the measured fracture toughness and a random function of ξ.

As well known, body waves travel faster than surface waves, which means body waves and surface waves can be separated from the field measured vibration data. When the field monitoring points are sufficiently far away from the blasting source, the influence of the curvature of wavefront

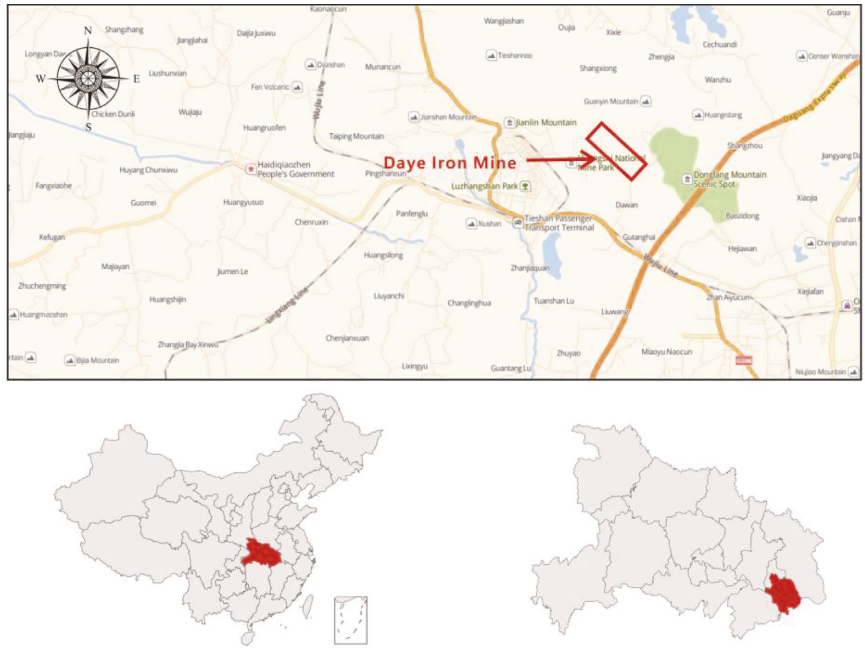

Figure 3: Location of Daye iron mine.

can be neglected and regarded as a plane wave. Consequently, the PPV on the wavefront is the same and we can measure the PPV on the wavefront by common equipment to determine whether the slope is stable or not when the blasting seismic wave arrives at the fracture tip.

3. Numerical Results and Discussions

3.1. General Description. A large iron reserve is located in Tieshan district, Daye city, Hubei Province in central China, which consists of 6 large-scale ore bodies with a maximum length of up to 920 m. Figure 3 shows the location of the site. The surface mining at the east open pit completed in 2005 and since then the underground mining has been adopted, leaving a pit spanning across 2400 m from east to west and 1000 m from south to north. The maximal vertical difference of height is up to 444 m and the maximal slope angle as is great as 53°, as shown in Figure 4. For sake of production safety, the slope must be ensured on the side of stability.

According to geological investigations, a lot of faults of distinct scales exist at this site, in which the faults F9 and F9′ control the stability of the northern slope, generally acknowledged with a least stability, as shown in Figure 5. The blasting excavation is beneath the bottom. Calculations show that the incident angle γ_1 of induced blasting waves varies from 0 to 8o at the tip of F9′ and from 48° to 60° at the tip of F9.

There is no doubt that the PPV threshold (v_{SV}) is dependent on the mechanical parameters of rock mass and the property of incident waves. In general, the variation of measured density (ρ) is small enough to be negligible while the variations of measured mode I fracture toughness (K_{IC}), Young's modulus (E), and Poisson's ratio (υ) are impossible to ignore, which can be well fitted by the normal distribution function [17]. K_{IC} was measured in Reference [18], whose mean value is about 1 MPa•m$^{1/2}$ and the coefficient of variation (CV) is no greater than 0.2 [19]. Other parameters of rock mass are given by Huang et al. and Jiang et al. [20, 21]. The mean values of ρ, E, and υ are 2710 kg/m^3, 18.37 GPa, and 0.23, respectively. The CVs of E (δ_E) and υ (δ_υ) are less than 0.2 and 0.1, respectively.

3.2. PPV Threshold Analysis Using Deterministic Method. In this section, the mean values of K_{IC}, E, and υ are taken in the following analysis. The variations of v_{SV} and θ_0 with respect to the incident wave frequency (f) and the incident angle (γ_1) are plotted in Figure 6.

It can be seen that for a fixed γ_1, v_{SV} increases monotonically with the increasing f, which is in line with the well-known results. v_{SV} peaks at $\gamma_1 = 45^o$ and falls to the lowest point at around $\gamma_1 = 14^\circ$. The least v_{SV} increases from 3.38 cm/s to 15.11 cm/s when f increases from 10 Hz to 200 Hz. The PPV criterion should be determined on the safe side and the least v_{SV} proposed. According to the Blasting Safety Regulation (GB6722-2014) in China, the frequency is always divided into 3 intervals and the corresponding PPV criterion determined as 3.38 cm/s for $f \leq 10$ Hz, as 3.38 cm/s-7.55 cm/s for 10 Hz $< f \leq 50$ Hz, and as 7.55 cm/s-15.11 cm/s for $f > 50$ Hz.

θ_0 shares exactly the same trend as f varies, indicating there is no influence of f on θ_0. θ_0 keeps negative except at $\gamma_1 = 45^\circ$, implying that the cracking is towards the free surface. Consequently, a through structural surface is likely to occur inside the northern slope once the PPV exceeds the proposed threshold. Overall, the blasting vibration must be strictly controlled and some vibration absorption measures are necessary.

3.3. PPV Threshold Further Analysis Using Probabilistic Method. If the PPV threshold in Section 3.2 is accepted, we have no information about the probability of failure of the northern slope. In a bid to obtain a probability measure of

Figure 4: Bird's eye view of the east open pit.

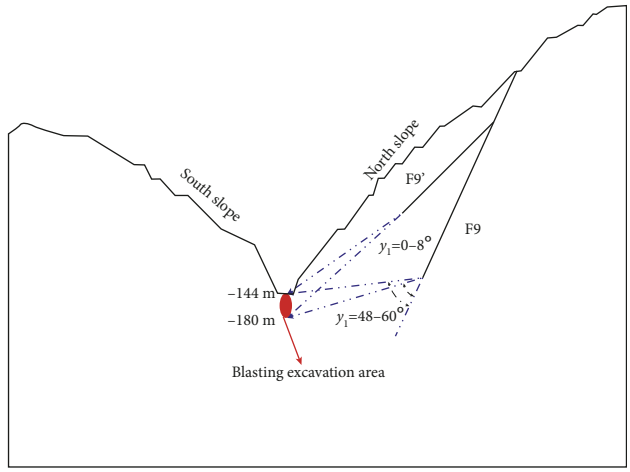

Figure 5: Typical profile of slope controlled by faults F9 and F9'.

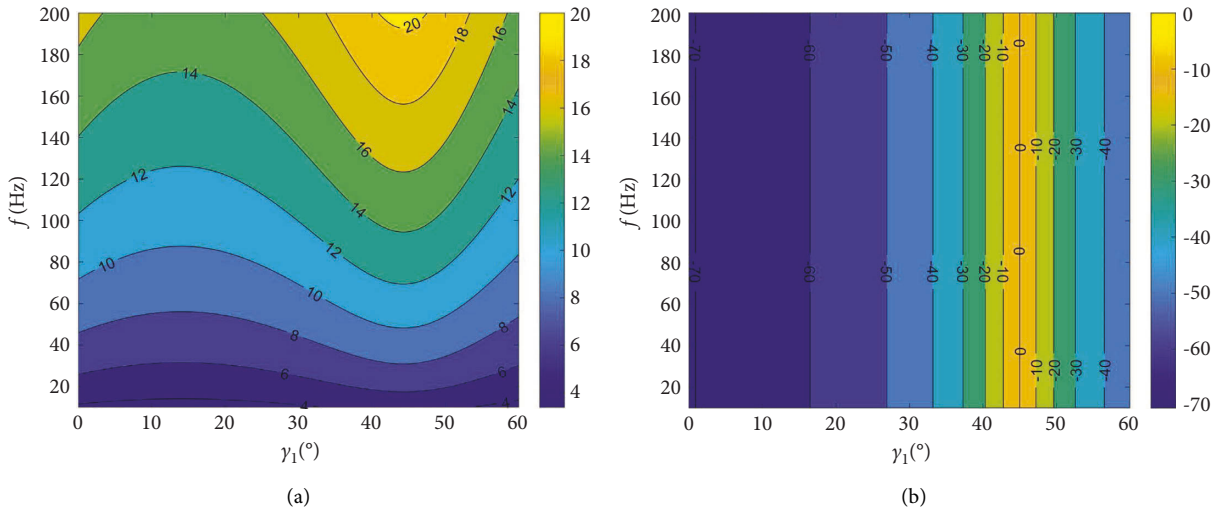

Figure 6: Contours of evaluated v_{SV} and θ_0 when mean values of parameters are taken. (a) v_{SV} and (b) θ_0.

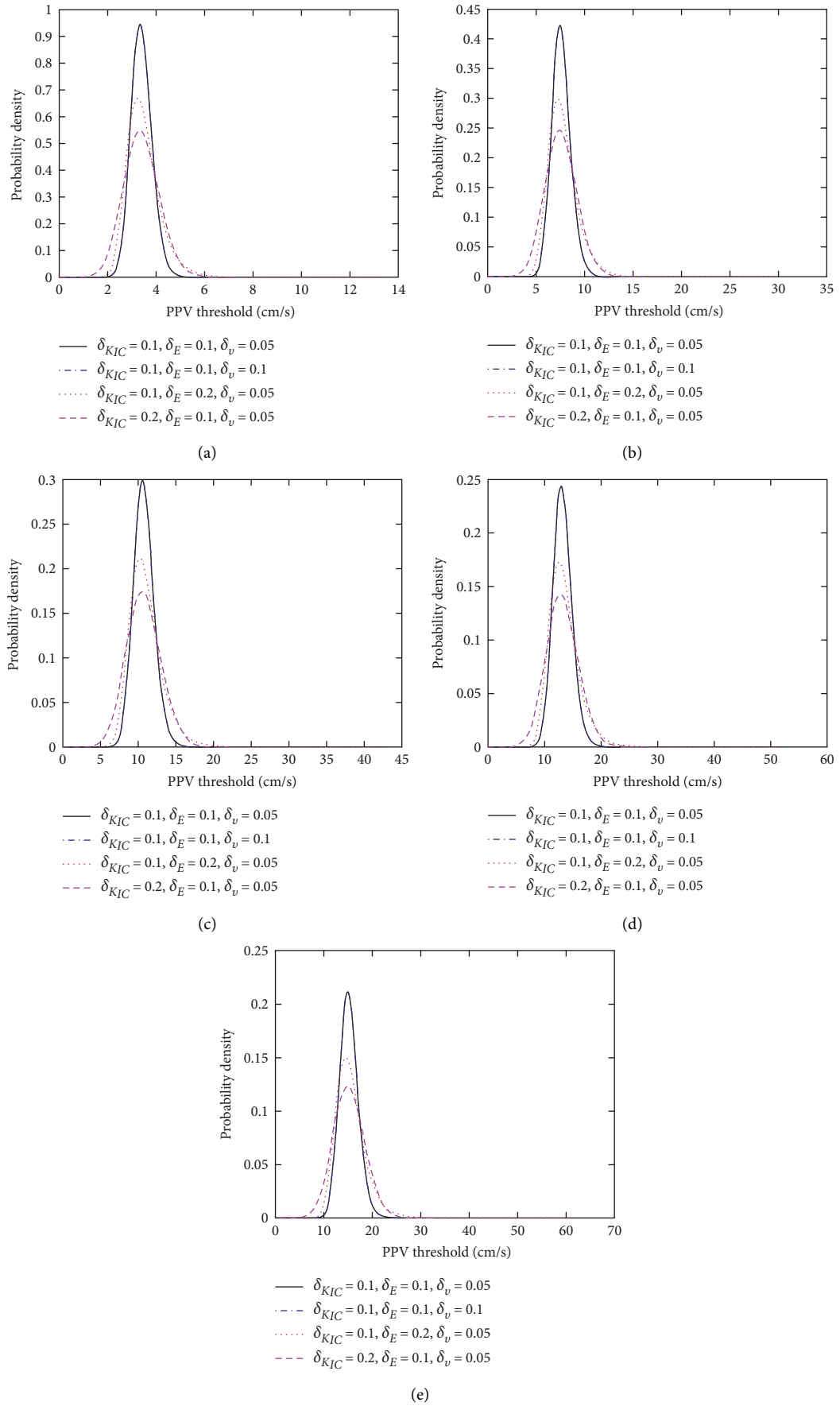

Figure 7: PDF of PPV threshold for different frequencies. (a) 10 Hz, (b) 50 Hz, (c) 100 Hz, (d) 150 Hz, and (e) 200 Hz.

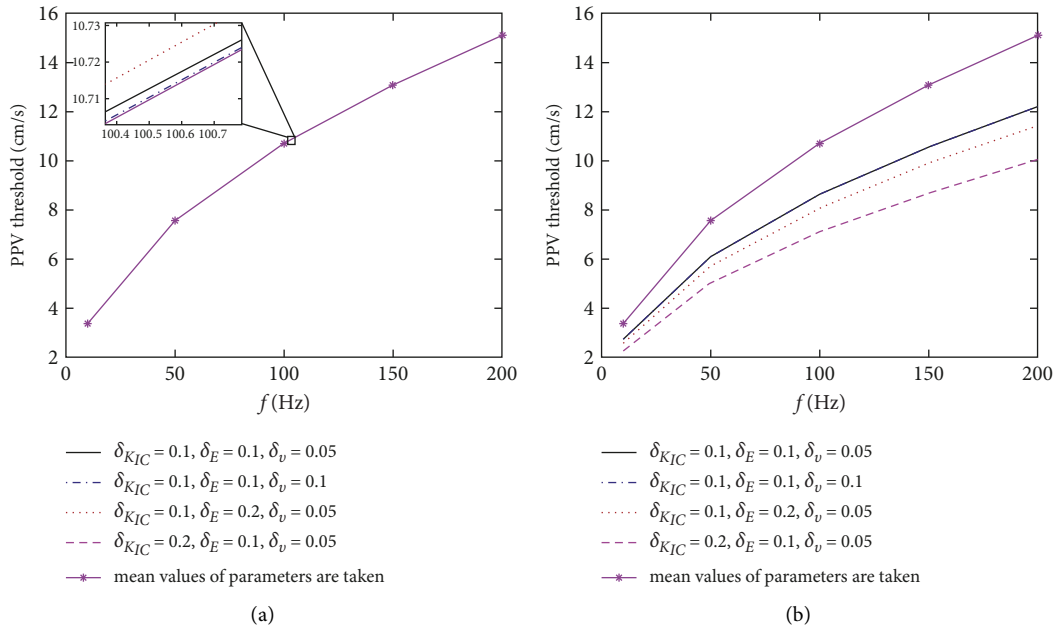

Figure 8: PPV thresholds with different failure probabilities. (a) 50% failure probability and (b) 5% failure probability.

failure, the variation of mechanical parameters of rock mass should be taken into consideration. In this section, the influences of the variations of K_{IC}, E, and υ on v_{SV} will be investigated.

The probability density functions (PDFs) of PPV threshold for the cases of $f = 10$ Hz, 50 Hz, 100 Hz, 150 Hz, and 200 Hz are plotted in Figure 7. The case of $\delta_E = \delta_{K_{IC}} = 0.1$ and $\delta_\upsilon = 0.05$ acts as the reference.

It can be observed that all the unimodal curves are slightly positively skewed, meaning that the modes are a little less than the mean values, that is, as high as 5.26% (caused by the increment of δ_E) and as low as 0.48% (caused by the increment of $\delta_{K_{IC}}$). According to the requirement of engineering precision, the modal and the mean values can be regarded as the same.

For each frequency, the PDF varies in a similar way. When δ_υ increases from 0.05 to 0.1, all the PDF curves almost coincide, implying the CV of PPV threshold is nearly unchanged and the PPV threshold is insensitive to υ. However, when δ_E and $\delta_{K_{IC}}$ rise from 0.1 to 0.2, the modes change slightly, that is, only less than 2% as compared to the reference, while the PDF curves become shorter and wider indicating a higher spread in PDF. We can claim that E and K_{IC} are the primary factors influencing the variation of PPV threshold, which are in accordance with the results of PPV criterion analysis by Lu et al. [13].

Figure 8 depicts the proposed PPV thresholds with 50% and 5% failure probabilities, as compared with that in Section 3.2.

It can be seen in Figure 8(a) that all the curves essentially coincide with each other, indicating the results in Section 3.2 with a failure probability as high as 50%. This is absolutely unacceptable in engineering practice. Therefore, a more rigorous PPV threshold should be determined. Generally, an event is accepted as a tiny-probability one with a failure probability as low as less than 5%. As a consequence, the PPV threshold with 5% failure probability should be given. It can be observed in Figure 8(b) that the PPV threshold reaches the lowest as $\delta_{K_{IC}} = 0.2$. The proposed PPV criterion is determined as 2.25 cm/s for $f \leq 10$ Hz, as 2.25 cm/s-5.02 cm/s for $10\text{ Hz} < f \leq 50$ Hz, and as 5.02 cm/s-10.05 cm/s for $f > 50$ Hz.

4. Conclusions

The fault is considered as a semi-infinite crack in an unbounded space, and the SV component of blasting waves is simplified as a plane wave to investigate the dynamic responses of a rock slope. A theoretical solution of PPV threshold is derived, and the slope stability is evaluated using two methods—deterministic and probabilistic methods.

The PPV threshold increases monotonically with the increasing frequency and reaches the lowest point at around $\lambda_1 = 14^\circ$, which should be proposed as the PPV threshold. After investigating the influence of the variations of mechanical parameters, the PPV threshold is with a 50% failure probability when the mean values of mechanical parameters are taken. On the safe side, a more rigorous PPV threshold with only 5% failure probability is determined as 2.25 cm/s for $f \leq 10$ Hz, as 2.25 cm/s-5.02 cm/s for $10\text{ Hz} < f \leq 50$ Hz, and as 5.02 cm/s-10.05 cm/s for $f > 50$ Hz, which are far smaller than those of intact rock slopes. Due to the negative initiation angles, a through structural surface is likely to occur inside the northern slope once the PPV exceeds the proposed threshold.

4.1. Limitations and Future Works. The result in this manuscript is based on the linear elastic fracture dynamics, in which the blasting seismic wave is treated as a signal which will interact with the fault and cause dynamic stress field. The strain rate only causes a different dynamic stress

field, and its influence on the change of rock property cannot be considered. In the future research, we will adopt the nonlinear fracture dynamic to take strain rate into consideration.

Abbreviations

PPV: Peak particle velocity
$\psi^{(i)}$: Potential function of the incident SV-wave
γ_1: Incident angle
ψ_0: Amplitude of the incident SV-wave
$\alpha_{1,2}$: Wave number of SV- and P-waves
ω: Circular frequency
$c_{1,2}$: Wave speed of SV- and P-waves
λ, μ: Lame's constants
ξ: Random variable
ρ: Density of rock mass
E: Young's modulus
υ: Poisson's ratio
i: Unit of complex
$\psi^{(d)}, \varphi^{(d)}$: Potential functions of diffracted SV- and P-waves
$\psi^{(s)}, \varphi^{(s)}$: Potential functions of symmetric parts of diffracted SV- and P-waves
$\psi^{(a)}, \varphi^{(s)}$: Potential functions of antisymmetric parts of diffracted SV- and P-waves
K_I, K_{II}: Stress intensity factor of type I and type II
K_{IC}: Measured fracture toughness
θ°: Initiation angle
σ_{ij}: Components of stress tensor
$\delta_E, \delta_\upsilon, \delta_{K_{IC}}$: Coefficients of variation of E, υ, and KIC
v_{SV}: PPV threshold
PDF: Probability density function.

Data Availability

The data used to support the findings of this study are included within the article.

Conflicts of Interest

The authors declare that there are no conflicts of interest regarding the publication of this article.

Acknowledgments

The study was sponsored by Hubei Provincial Natural Science Foundation (2021CFB541, 2019CFB224), Hubei Provincial Department of Education (Q20191308), National Natural Science Foundation of China (42102329), and Open Research Fund of Hubei Key Laboratory of Blasting Engineering (HKLBEF202011).

References

[1] X. Feng, Q. Jiang, X. Zhang, and H. Zhang, "Shaking table model test on the dynamic response of anti-dip rock slope," *Geotechnical & Geological Engineering*, vol. 37, no. 3, pp. 1211–1221, 2019.

[2] J. Huang, M. Zhao, C. Xu, X. Du, L. Jin, and X. Zhao, "Seismic stability of jointed rock slopes under obliquely incident earthquake waves," *Earthquake Engineering and Engineering Vibration*, vol. 17, no. 3, pp. 527–539, 2018.

[3] K. R. Perth, D. Choudhury, and K. Bhargava, "Simulation of rock subjected to underground blast using FLAC3D," *Japanese Geotechnical Society Special Publication*, vol. 2, pp. 508–511, 2016.

[4] G. Fan, L. Zhang, X. Li, R. Fan, and J. Zhang, "Dynamic response of rock slopes to oblique incident SV waves," *Engineering Geology*, vol. 247, pp. 94–103, 2018.

[5] R. S. Ganjeh, H. Memarian, M. H. Khosravi, and M. Mojarab, "A comparison between effects of earthquake and blasting on stability of mine slopes: a case study of Chadormalu open-pit mine," *Journal of Mining and Environment*, vol. 10, pp. 223–240, 2019.

[6] Y. Zhang, G. Chen, J. Wu, Z. Lu, and X. Zhuang, "Numerical simulation of seismic slope stability analysis based on tension-shear failure mechanism," *Geotechnical Engineering*, vol. 43, pp. 18–28, 2012.

[7] Y. r Liu, Z. He, K. d Leng, Y. q Huang, and Q. Yang, "Dynamic limit equilibrium analysis of sliding block for rock slope based on nonlinear FEM," *Journal of Central South University*, vol. 20, no. 8, pp. 2263–2274, 2013.

[8] D. Deb, K. N. R. Kaushik, B. H. Choi, C. H. Ryu, Y. B. Jung, and C. Sunwoo, "Stability assessment of a pit slope under blast loading: a case study of Pasir coal mine," *Geotechnical & Geological Engineering*, vol. 29, no. 4, pp. 419–429, 2011.

[9] C. H. Dowding and C. Gilbert, "Dynamic stability of rock slopes and high frequency traveling waves," *Journal of Geotechnical Engineering*, vol. 114, no. 10, pp. 1069–1088, 1988.

[10] K. Kong, "Blasting vibration assessment of rock slopes and a case study," in *Proceedings of the 2013 International Symposium on Slope Stability in Open Pit Mining and Civil Engineering*, Nedlands, W.A, September 2013.

[11] S. Li, T. He, and X. Yin, *Rock Facture Mechanics*, Springer, Vienna, Austria, 2016.

[12] G. Simangunsong and S. Wahyudi, "Effect of bedding plane on prediction blast-induced ground vibration in open pit coal mines," *International Journal of Rock Mechanics and Mining Sciences*, vol. 79, pp. 1–8, 2015.

[13] S. Lu, C. Zhou, Z. Zhang, L. Ji, and N. Jiang, "PPV criterion of a rock slope imbedded with a fault subjected to blasting P-waves," *Shock and Vibration 2020*, vol. 2020, Article ID 8865981, 7 pages, 2020.

[14] S. Lu, C. Zhou, Z. Zhang, and N. Jiang, "Particle velocity response of surrounding rock of a circular tunnel subjected to cylindrical P-waves," *Tunnelling and Underground Space Technology*, vol. 83, pp. 393–400, 2019.

[15] V. G. Daniele and R. S. Zich, *The Wiener-Hopf Method in Electromagnetics*, SciTech Publishing, New York, NY, USA, 2014.

[16] B. Noble, *Methods Based on the Wiener-Hopf Technique for the Solution of Partial Differential Equations*, Pergamon Press, New York, NY, USA, 1958.
[17] S. Lu, H. Zhang, and L. Ji, "Random dynamic response characteristics of pipeline subjected to blasting cylindrical SH waves," *Shock and Vibration*, vol. 2021, Article ID 5592858, 9 pages, 2021.
[18] L. Li, H. Ning, F. Xu, J. Wang, H. Li, and L. Hou, "Test and numerical analysis of fracture toughness mdel III fracture Chinese," *Journal of Rock Mechanics and Engineering*, vol. 25, pp. 2523–2528, 2006.
[19] Z. Cui, D. Liu, G. An, M. Zhou, and Z. Li, "Research for determining mode I rock fracture toughness K_(IC) using cracked chevron notched Brazilian," *Disc Specimen Rock and Soil Mechanics*, vol. 31, pp. 2743–2748, 2010.
[20] Y. Huang, D. Liu, Z. Cheng, B. Liu, and Y. Feng, "Experimental on mechanical properties of diorite," *Journal of Liaoning Technical University*, vol. 32, pp. 1066–1070, 2013.
[21] N. Jiang, C. Zhou, S. Lu, and Z. Zhang, "Propagation and prediction of blasting vibration on slope in an open pit during underground mining," *Tunnelling and Underground Space Technology*, vol. 70, pp. 409–421, 2017.